modelling

MDPI

Article

High-Throughput Numerical Investigation of Process Parameter-Melt Pool Relationships in Electron Beam Powder Bed Fusion

Christoph Breuning *, Jonas Böhm, Matthias Markl and Carolin Körner

Chair of Materials Science and Engineering for Metals, Friedrich-Alexander-Universität Erlangen-Nürnberg, Martensstr. 5, 91058 Erlangen, Germany

* Correspondence: christoph.breuning@fau.de

Abstract: The reliable and repeatable fabrication of complex geometries with predetermined homogeneous properties is still a major challenge in electron beam powder bed fusion (PBF-EB). Although previous research identified a variety of process parameter–property relationships, the underlying end-to-end approach, which directly relates process parameters to material properties, omits the underlying thermal conditions. Since the local properties are governed by the local thermal conditions of the melt pool, the end-to-end approach is insufficient to transfer predetermined properties to complex geometries and different processing conditions. This work utilizes high-throughput thermal simulation for the identification of fundamental relationships between process parameters, processing conditions, and the resulting melt pool geometry in the quasi-stationary state of line-based hatching strategies in PBF-EB. Through a comprehensive study of over 25,000 parameter combinations, including beam power, velocity, line offset, preheating temperature, and beam diameter, process parameter-melt pool relationships are established, processing boundaries are identified, and guidelines for the selection of process parameters to the achieve desired properties under different processing conditions are derived.

Keywords: additive manufacturing; thermal modeling; electron beam powder bed fusion; processing window; scaling laws

Citation: Breuning, C.; Böhm, J.; Markl, M.; Körner, C. High-Throughput Numerical Investigation of Process Parameter-Melt Pool Relationships in Electron Beam Powder Bed Fusion. *Modelling* **2023**, *4*, 336–350. https://doi.org/10.3390/modelling4030019

Academic Editor: Kumar K. Tamma and Abílio M.P. De Jesus

Received: 25 April 2023
Revised: 19 June 2023
Accepted: 4 July 2023
Published: 10 July 2023

1. Introduction

Electron beam powder bed fusion (PBF-EB) is an additive manufacturing process that uses a high-energy electron beam for the local consolidation of metal powder. Layerwise build-up enables the tool-free fabrication of complex geometries, with few geometrical restrictions [1,2]. High-vacuum conditions, in combination with high process temperatures and the ability to tailor the spatiotemporal energy input, enable the processing of a large variety of metal alloys [3–9] and even the local tailoring of microstructure and properties [10–14]. The selection of appropriate process parameters in PBF-EB is critical for the fabrication of defect-free parts with predetermined homogeneous material properties.

In general, the process parameters for part fabrication are selected from material-specific process parameter maps, which relate processing parameters to density, surface morphology, and relevant mechanical and functional properties. Using the classical approach, process parameter maps can be established using the fabrication of standardized cuboid specimens and their subsequent classification according to their density and surface morphology [15–18]. The advent of reliable in situ process observation using electron optical imaging (ELO) opened the possibility of the in situ identification and classification of sample surfaces, requiring only a limited number of representative layers for each parameter combination, and thereby enabled a significant reduction in the time investment required [19,20]. A further simplification of the process parameter development is possible with the application of advanced interpolation algorithms, which are able to predict the

properties of any given process parameter based on a reduced number of experimental sampling points, while still representing the ground truth with minimum error [21–24]. Aoyagi et al. showed the possibility of obtaining a reliable processing map based on only a limited amount of process parameter combinations [25]. Pure experimental approaches establish the relationship between process parameters and final material properties using an end-to-end approach, thereby disregarding the underlying thermal conditions and the emerging melt pool geometry. End-to-end approaches may be sufficient for the fabrication of the same sample geometry under the same processing conditions, but are not suitable for the transfer of desired properties to complex geometries and variable processing conditions, since the final material properties are governed by the local thermal conditions, instead of the local process parameters.

Recent developments combining numerical and experimental approaches have established melt pool geometry–property relationships, e.g., by relating local variations in the surface morphology to local changes in the melt pool geometry [26–28]. In addition, the extension of line-based scanning strategies to integrating return time compensation has enabled the fabrication of complex geometries with a homogeneous melt pool geometry, which is equivalent to the melt pool geometry emerging in the quasi-stationary state of a cuboid [29]. Therefore, the fabrication of complex geometries with predefined, homogeneous properties is reduced to two independent steps. First, the identification of the required melt pool geometry, which results in the desired properties, according to the melt pool geometry–property relationships. Second, the selection of appropriate process parameters, according to process parameter–melt pool geometry relationships, which form the required melt pool geometry under the present processing conditions. Therefore, process parameter–melt pool geometry relationships and their dependencies on processing conditions are crucial for the selection of suitable parameter combinations and the transfer of properties between different geometries, processes, and PBF-EB machines with different specifications.

The spatiotemporal melt pool evolution and the dependencies underlying the process parameter–melt pool geometry relationships are, however, not easily accessible. Therefore, numerical simulations can provide an insight into the melt pool geometry, as a function of different process parameters and conditions [30–33]. High-fidelity models that resolve individual powder particles depict the thermo- and hydrodynamics of the melt pool, offer the possibility of precisely describing the governing physical processes, predict process parameter relationships, and determine processing boundaries. These models are, however, computationally expensive and have to be limited to two dimensions, in order to determine melt pool geometries for a large number of process parameter combinations [34–36]. Simplified thermal models, in contrast, neglect the effects of fluid convection, evaporation, and radiation but enable the efficient simulation of the spatiotemporal evolution of temperature fields and melt pool geometries with an accuracy sufficient for making predictive statements [11,37–39]. Several studies have focused on the determination of relationships between the melt pool geometry and process parameters in laser powder bed fusion and identified dimensionless numbers, to generalize the underlying relationships [40–42]. These studies, however, only considered the melt pool geometry of single melt tracks and did not take the influence of neighboring melt tracks into account, which govern melt pool formation in PBF-EB.

The objective of this work was to establish fundamental relationships between process parameters, processing conditions, and the melt pool geometry in the quasi-stationary state of line-based hatching strategies in PBF-EB, as a foundation for process parameter selection and the transfer of melt pool geometries. For this purpose, melt pool geometries for a multitude of parameter combinations were determined for the model material Ti6Al4V using high-throughput numerical simulations, and the corresponding processing boundaries and their dependencies on different processing conditions were established.

2. Methods

In order to obtain relationships between process parameters, processing conditions, and the emerging melt pool geometry in the quasi-stationary state of cuboid geometries, a comprehensive study of melt pool geometries was conducted for a variety of parameter combinations and processing conditions, using the model material Ti6Al4V. The quasi-stationary state of any hatch with constant line length is reached when the cumulative heating effect converges to its highest value and constant thermal conditions for melt pool formation are reached [27]. For the calculation of the corresponding temperature distributions in the quasi-stationary state for each parameter combination, a semi-analytical heat conduction model was implemented. This model disregarded fluid convection, latent heat release, radiation, and vaporization but enabled efficient, parallel computation and produced promising results in the prediction of melt pool geometries [26,39,43]. Compared to high-fidelity models, when considering these effects, a simplified model can lead to small changes in the melt pool geometry and consequently the location of the processing boundaries [44]. However, the trends underlying the influence of process parameter variations and processing conditions are preserved. The temperature T at time t and position x, y, z was based on an analytical solution for the transient temperature response [45] to a moving volumetric Gaussian heat source and was defined by

$$\begin{aligned} &T(t,x,y,z) - T_{preheat} \\ &= \frac{2\eta P}{c_p \rho (\pi/3)^{3/2}} \int_0^t \frac{1}{\sqrt{\phi_x \phi_y \phi_z}} exp\left(-\frac{3x(t')^2}{\phi_x} - \frac{3y(t')^2}{\phi_y} - \frac{3z(t')^2}{\phi_z}\right) dt' \end{aligned} \tag{1}$$

with

$$\phi_i = 12\alpha\left(t - t'\right) + \sigma_i^2 \qquad for \;\; i = x, y, z \tag{2}$$

where $T_{preheat}$ describes the preheating temperature, P is the beam power, η the absorption coefficient, ρ the density, and c_p the specific heat. The shape of the Gaussian beam is defined in each dimension with a beam width σ_i, corresponding to the full-width half maximum (FHWM) of the Gaussian distribution, and the thermal diffusivity α according to Equation (2). The motion of the heat source is described by the coordinate system, where $x(t'), y(t'), z(t')$ describe the distance from the point of interest to the transient location of the beam at time t'. The piece-wise definition of scan paths prohibited the analytical integration of Equation (1). Therefore, the Gaussian quadrature scheme proposed by B. Stump et al. was used to numerically integrate the temperature at a given time and location [38]. The material parameters were assumed to be constant and uniform. The estimated material parameters for Ti6Al4V adapted from Rausch et al. are summarized in Table A1 [34,46–48]. For the computation of a large amount of parameter combinations, the model was implemented using *numpy* [49] and *mpi4py* [50] for an efficient parallel evaluation.

For the calculation of material specific melt pool feature maps, a step-wise procedure was necessary, which is detailed in Figure 1. Melt pool feature maps relate characteristic melt pool features to each point in the parameter space and enable the determination of the influence of different processing conditions and process strategies on the location and extension of the processing map, where defect-free fabrication is possible. Within the scope of this study, the parameter space was defined by variations of the process parameters; power P and velocity v; variations of the geometry and hatching strategy, line length l_m and line offset l_o; and variations of processing conditions, ambient preheating temperature $T_{preheat}$, and beam diameter σ. For the comparison between different parameters of the process parameter space, the melt pool feature maps were calculated as a function of the area energy ($E_a = P/v \cdot l_o$) and lateral velocity ($v_{lat} = v \cdot l_o/l_m$). While the beam velocity describes the velocity in the direction of the hatch vectors, as indicated in Figure 1d, the lateral velocity describes the velocity in the lateral direction over the course of the hatch.

A summary of the process parameter space, base values used as reference, and their corresponding range of variation can be found in Table 1.

Table 1. Properties of the process parameter space with corresponding reference values and variation ranges.

Property	Unit	Base Value	Range
Area Energy	J/mm²	/	[0.6 . . . 2.2, 0.1]
Lateral Velocity	mm/s	/	[2 . . . 149.5, 2.5]
Line Offset	µm	100	[30, 100, 150]
Scan Length	mm	15	[10, 15, 20, 30]
Beam Diameter (FWHM)	µm	200	[150, 200, 400]
Preheating Temperature	K	1023	[973, 1023, 1073, 1123]

For each point of interest in the parameter space (Figure 1a) the characteristic melt pool geometry in the quasi-stationary state had to be calculated. For this purpose, a simulation domain in the quasi-stationary state of the hatch with a spatial discretization of $dx = 10\,\mu m$ was established and the temperature fields of three consecutive melt lines were calculated according to Equation (1) for each parameter combination in 100 discrete time steps t_i (Figure 1b). For each time step, the melt pool envelope was determined according to the liquidus temperature T_l and the respective melt pool features were identified in the region of interest, as marked in Figure 1d. The features of interest were, as indicated in Figure 1c, the maximum melt pool depth, the melt pool lifetime, and the aspect ratio of the melt pool. The characteristic melt pool features $\lambda_n = max(\lambda_{t_i})$ of a parameter combination n were subsequently determined from the maximum of each quantity over each time step t_i. Melt pool feature maps combined each characteristic feature for all parameter combinations and were represented as a two-dimensional slice, along the area energy E_A and lateral velocity v_{lat} axis, through the multidimensional parameter space, analog to experimental representations [51], as detailed in Figure 1e. Since the area energy E_A and the lateral velocity v_{lat} are the quantities governing the cumulative heating process underlying melt pool formation in line-based hatching strategies, this representation provided the possibility of establishing the underlying relationship between process parameters and the investigation of the influence of different processing conditions. In order to determine the final processing maps (Figure 1f), three processing boundaries were identified according to different geometric thresholds that had been identified in previous research and are indicated in Figure 1e. The consolidation boundary marks the lower bound of the processing map, ensuring sufficient connection between subsequent layers [34]. Several factors, including the melt pool depth and the distance between adjacent melt lines, determined the consolidation. Within the scope of this study, however, sufficient connection was assumed when the melt pool depth exceeded the effective layer thickness [34]. From the nominal layer thickness of $h_0 = 50\,\mu m$, and a powder bulk density of 50%, the effective layer thickness could be calculated as 100 µm. Based on the relationship between the melt pool lifetime and the beam return time, the melt pool could be separated into a trailing melt pool regime, where the melt pool is already solidified when the beam returns, or a persistent melt pool, where the melt pool is still liquid when the beam returns [27]. The persistence boundary separates the trailing and persistent regions of the processing map and is defined by the onset of a permanent persistent melt pool and its associated change in material transport conditions [27]. For particular parameters, the located in the transition region between the trailing and permanent persistent melt pool are prone to the formation of bulged melt surfaces, due to inhomogeneous material transport conditions. The position of the melt pool stability limit defines the upper limit of the processing map and is reached when the aspect ratio between lateral melt pool extension l_e and melt pool depth d exceeds a predefined value $l_e/d \geq 4.7$ [26].

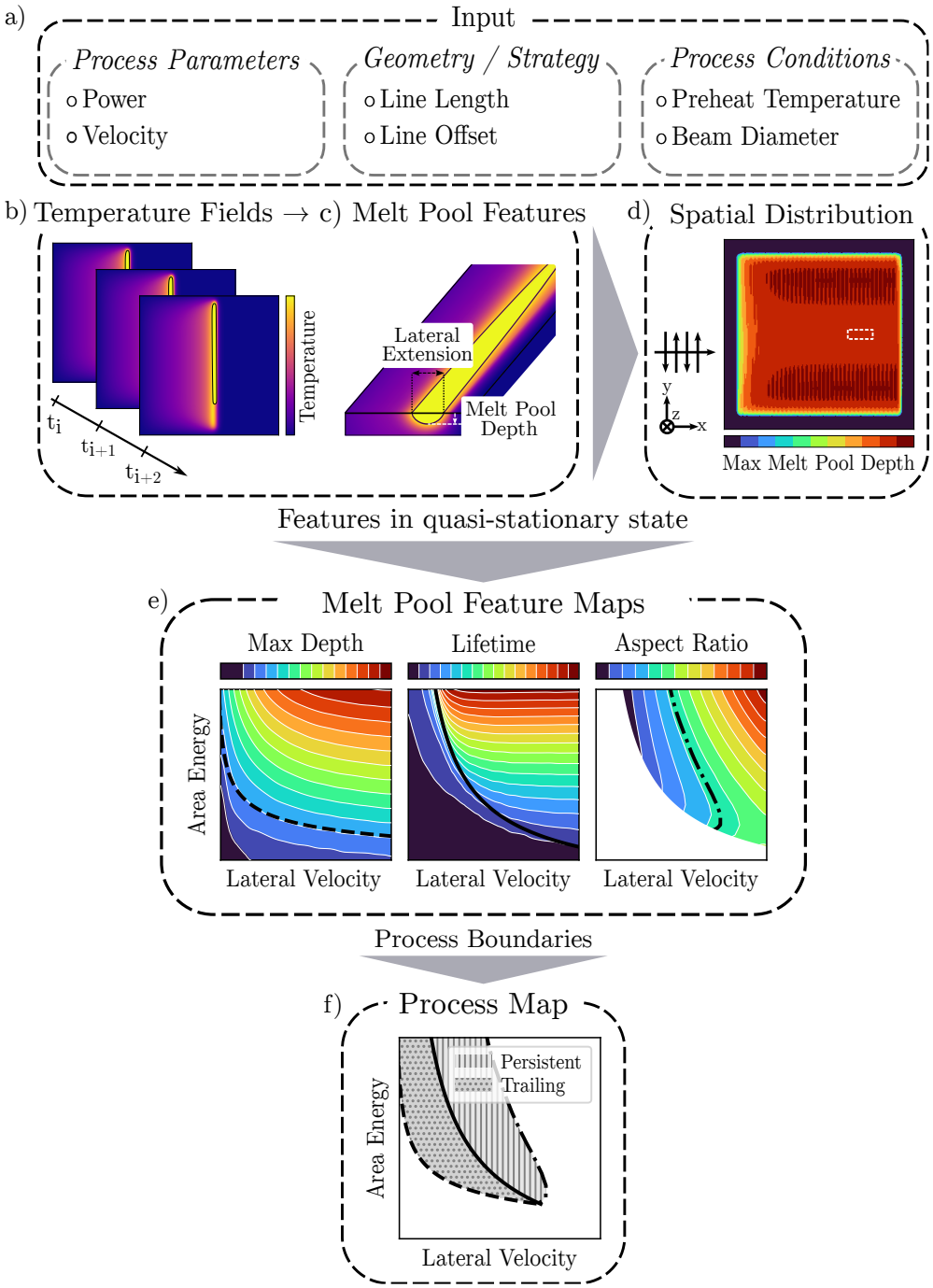

Figure 1. Procedure for obtaining processing maps from the computed temperature fields as a function of the different input parameters; (**a**) input parameters; (**b**) calculated temperature fields and (**c**) extracted melt pool features; (**d**) spatial distribution of melt pool features with area of interest in the quasi-stationary region; (**e**) melt pool feature maps combining features for different input parameters; (**f**) identification of process map using processing boundaries.

3. Results and Discussion

3.1. Process Parameters

Prior to determining the influence of the different processing conditions on the melt pool geometry, the underlying relationships between the different process parameters and the emerging melt pool geometry had to be established as a baseline reference. Figure 2 shows the calculated melt pool feature maps as a function of the area energy and lateral

velocity, the derived process boundaries, and the final processing map. A variety of dependencies were observed, in accordance with previous experimental and numerical work [15,17,51]. The melt pool depth increased with a higher total energy input and constant lateral velocity and with a larger lateral velocity at a constant energy input. As a consequence, the consolidation boundary shifted towards lower energy inputs with a higher lateral velocity.

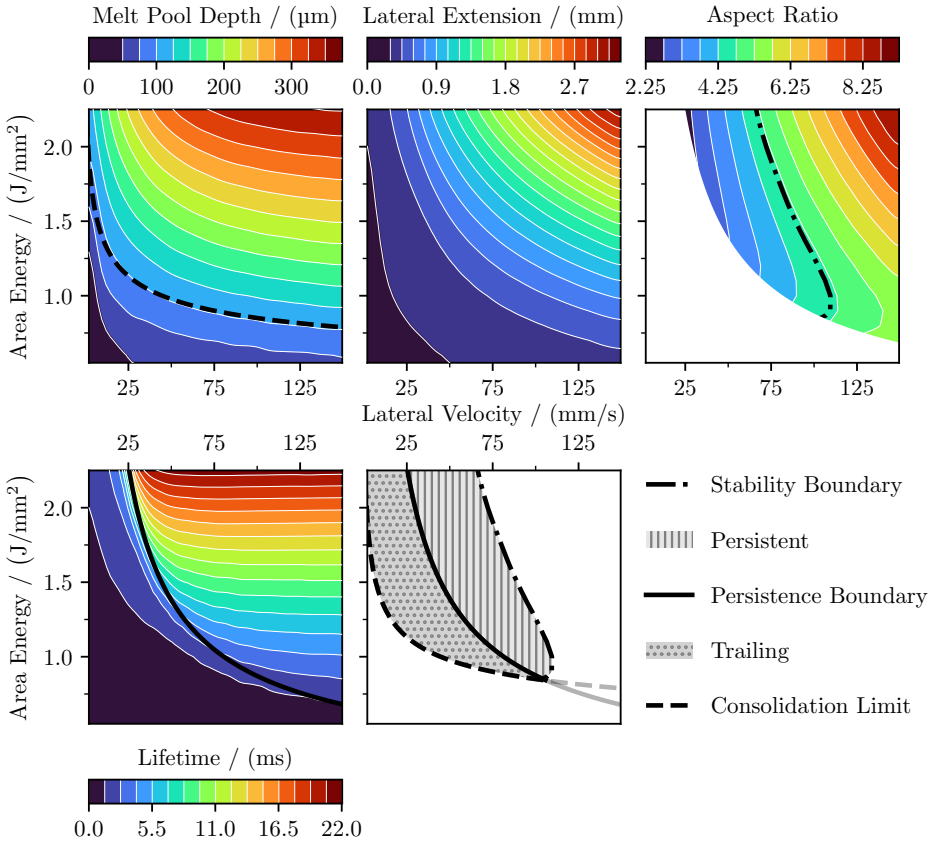

Figure 2. Melt pool geometry features of 1020 process parameter combinations calculated for area energies of 0.6 J mm^{-2} to 2.2 J mm^{-2} and lateral velocities of 2.5 mm s^{-1} to 149.5 mm s^{-1} with a line offset of 100 µm, line length of 15 mm, preheating temperature of 1023 K, and beam diameter of 200 µm. Melt pool depth (**top left**), melt pool lifetime (**bottom left**), lateral melt pool extension (**top center**), and melt pool aspect ratio (**top right**). The derived processing boundaries are indicated. Combination of processing boundaries in the final processing map (**bottom center**).

A similar pattern cold be observed for the location of the persistence boundary that emerged from the increase in the melt pool life time with higher energy inputs and lateral velocities. While a low lateral velocity required a higher energy input to form a persistent melt pool, the necessary energy input decreased for higher lateral velocities, due to the decreasing return time. This ultimately led to the intersection of the persistence and the consolidation boundary in Figure 2 (bottom center), where a persistent melt pool was required to exceed the consolidation boundary. The lateral extension of the melt pool only showed small variations in the trailing melt pool regime below the persistence boundary with an increasing energy input and lateral velocity, but increased rapidly upon exceeding the persistence boundary with a higher energy input and lateral velocity. The combination of the trends governing the melt pool depth and lateral extension of the melt pool led to the pattern underlying the melt pool aspect ratio, which was only calculated for persistent melt pools. The aspect ratio of the melt pool exhibited a minimum for persistent melt pools, which emerged from a combination of a high energy input and low lateral velocity, since they exhibited a high melt pool depth and low lateral extension. Since the lateral extension

increased rapidly with higher lateral velocities, the aspect ratio increased simultaneously, giving rise to an upper processing boundary and resulting in a shallow melt pool that extended over a large portion of the geometry. Beyond this boundary no process parameter combination could be identified that enabled the formation of a melt pool geometry within the processing boundaries.

The location of the processing boundaries and the extension of the processing map resulted from the different melt pool geometries emerging for each process parameter combination. The melt pool geometry emerging in the quasi-stationary state of line-based hatching strategies was governed by the combination of the cumulative heating effect from previous hatch lines and the energy deposited at the current hatch line. While the energy deposited at the current hatch line was determined solely by its own energy input, the cumulative heating effect was governed by the energy input of previous hatch lines and their respective thermal loss until the current hatch line. Since each point in the process parameter space represents a unique combination of these quantities, a unique melt pool geometry emerged for each point in the process parameter space. As detailed in Figure 2, the emerging melt pool geometries exhibited fundamental patterns. A higher lateral velocity decreased the return time and time for heat dissipation; therefore, the magnitude of the cumulative heating effect increased and the melt pool size increased, shifting the necessary energy for consolidation towards a lower energy [15,51,52]. A higher energy input directly affected the melt pool depth but also increased the energy deposited at previous hatch lines and, therefore, the magnitude of the cumulative heating effect. Both effects resulted in a characteristic increase in the melt pool depth towards higher energy inputs and lateral velocities. The same effects also naturally led to the formation of a persistent melt pool at higher lateral velocities, due to the increased melt pool lifetime exceeding the reduced return time [39]. Consequently, the required energy for the formation of a persistent melt pool decreased for higher lateral velocities and ultimately led to the formation of a persistent melt pool below the consolidation boundary, as observed in Figure 2 (bottom center). High melt pool lifetimes paired with low return times also resulted in the extension of the melt pool in lateral direction towards high energy inputs and lateral velocities [26]. Based on the patterns underlying the depth and the lateral extension of the melt pool, the aspect ratio of the melt pool increased towards lower energy inputs, due to a lower melt pool depth, and towards higher lateral velocities, due to the increasing lateral extension of the melt pool. As a result, the characteristic shape of the processing map, as shown in Figure 2, emerged.

3.2. Processing Conditions-Preheating Temperature

Figure 3 shows the calculated processing boundaries and the resulting processing map for different preheating temperatures, ranging from 973 K to 1123 K. With an increasing preheating temperature, the consolidation limit shifted towards lower area energies and lower lateral velocities. The same trend could be observed for the persistence boundary and the melt pool stability limit boundary. As a consequence, the location of the whole processing map shifted towards the lower left of the process parameter space.

In addition to the effects described in Section 3.1, the underlying preheating temperature affected the thermal conditions. A higher preheating temperature increased the thermal energy of the material and less additional energy was necessary to form the same melt pool geometry. As a result, the processing boundaries shifted towards lower area energies and lateral velocities, as shown in Figure 3. Since the local preheating temperature at a given position in a build job is currently not closely controlled, significant temperature differences, e.g., in the form of local heat accumulation, can occur over the course of a build job, due to the combination of the preheating theme, local geometric features, and the melting sequence of different geometries [53]. Therefore, the selection of appropriate process parameters to achieve the desired melt pool geometry is crucial. Depending on the location of the selected process parameter, a local variation of the preheating temperature shifts the processing boundaries within the process parameter space and can lead to local

process boundary violations for a process parameter that was stable at a different preheating temperature. Since a local shift of the preheating temperature is typically a continuous process, slight changes of the surface topography can be identified using state-of-the-art in situ monitoring approaches [19,54], and appropriate countermeasures can be taken. Based on the unambiguous relationship between each processing boundary and its characteristic features, the underlying defect origin can be clearly identified, and improved process parameters can be chosen, to form the original melt pool geometry based on a shifted processing map. A different approach to counteracting geometry-induced changes of the preheating temperature is the local adaptation of the preheating scheme to reach the same preheating temperature independently of the underlying geometry. It is, however, not trivial to control the preheating temperature as a function of complex geometries, and further research is necessary to develop appropriate adaptable preheating schemes.

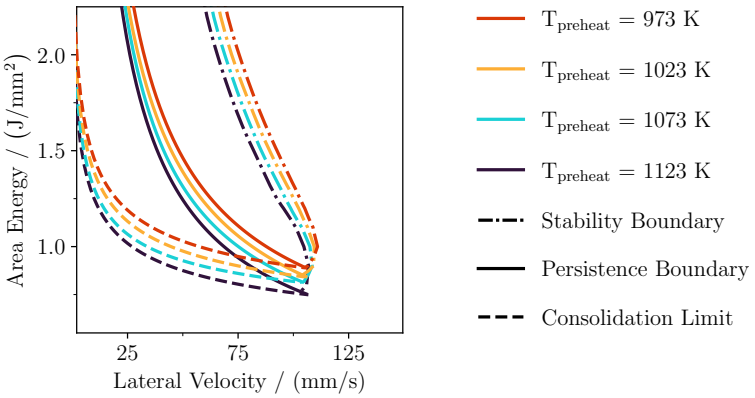

Figure 3. Processing boundaries for different preheating temperatures, ranging from 973 K to 1123 K for area energies of 0.6 J mm^{-2} to 2.2 J mm^{-2} and lateral velocities of 2.5 mm s^{-1} to 149.5 mm s^{-1} with line offset of 100 µm, line length of 15 mm, and beam diameter of 200 µm

3.3. Processing Conditions-Beam Diameter

As detailed in Figure 4, the melt pool depth, the location of the processing boundaries, and the resulting processing map were very sensitive to variations of the beam diameter. With a higher beam diameter, the consolidation boundary shifted towards higher area energies and lateral velocities. While the location of the persistence boundary did not change significantly, a change in the beam diameter had a significant influence on the location of the melt pool stability limit. At higher beam diameters, the melt pool stability limit retracted and wrapped towards the persistence line, resulting in its characteristic shape. While the melt pool depth generally decreased as the beam diameter increased, the effect was more pronounced at lower lateral velocities and area energies.

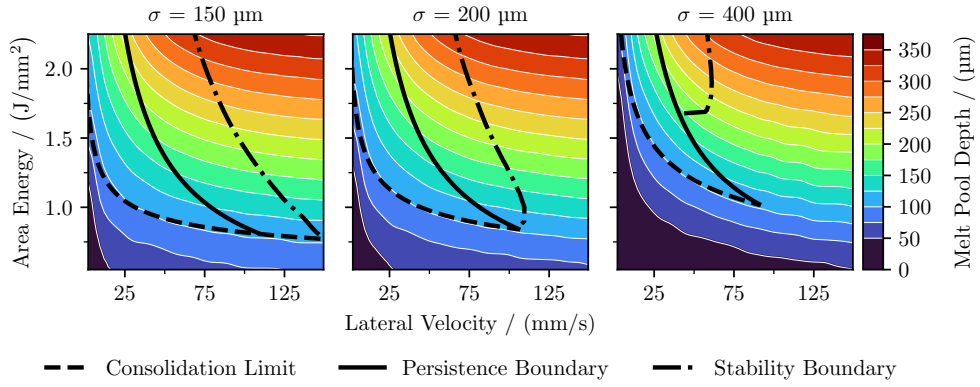

Figure 4. Melt pool depth distributions and process boundaries for different beam diameters (FWHM) of 150 µm, 200 µm, and 400 µm with area energies from 0.6 J mm^{-2} to 2.2 J mm^{-2} and lateral velocities from 2.5 mm s^{-1} to 149.5 mm s^{-1} at a line offset of 100 µm and line length of 15 mm.

The energy density distribution of the energy input was defined by the beam diameter of the electron beam [55]. With a larger beam diameter, the same amount of energy was deposited onto a larger area and the beam power density decreased. In the trailing melt pool regime, the melt pool formation was primarily governed by the energy input of the current line, and due to high return times, the cumulative heating effect only played a minor role. Therefore, overall, more energy was required to reach the same melt pool depth with larger beam diameters and the consolidation boundary shifted towards higher energy inputs and lateral velocities, as shown in Figure 4. At higher lateral velocities, the contribution of the cumulative heating effect increased and the melt pool formation was governed by the total energy input and return time, which were unaffected by variations in the beam diameter, and therefore the location of the persistence boundary was only slightly affected. However, the shape of the melt pool in the persistent region was affected significantly. Although the same amount of energy was deposited with larger beam diameters, it was deposited over a larger area and consequently a melt pool with lower depth but a higher lateral extension formed. This resulted in a significant shift of the melt pool stability limit towards the left and even the wrapping at lower energy inputs towards the persistence line, as shown in Figure 4 (right). Overall, the melt pool geometry and the location of the processing map was highly sensitive to variations of the beam diameter and the extension of the processing map was largest for low beam diameters. Therefore, knowledge of machine specific beam characteristics is crucial for an effective process parameter selection and the transfer of melt pool geometries between different PBF-EB machines.

3.4. Scan Length

Figure 5 (left) shows the calculated processing boundaries for different line lengths, from 10 mm to 30 mm. The location of each of the processing boundaries matched very well for each of the investigated line lengths in the calculated parameter range. The melt pool depth distribution of the two selected process parameter combinations in the trailing and persistent regime of the processing map, indicated by the two markers in Figure 5a, is shown for different line lengths in Figure 5b. The melt pool distributions exhibited the same melt pool depth at the center of the quasi-stationary state and the same characteristic increase in the melt pool depth towards the turning points of the hatch. The highest melt pool depth reached at the turning points was in good agreement for each of the investigated line lengths for each process parameter combination. However, the size of the return time effects, extending towards the center of the hatch, did not show the same size but instead increased for higher line lengths.

As detailed in Section 3.1, the melt pool geometry was governed by the present thermal conditions. While a constant area energy E_A ensured a constant total energy input, a constant lateral velocity v_{lat} ensured a constant mean beam return time $\overline{t_{ret}} = const.$, as shown in Figure 5c. Consequently, the magnitude of the cumulative heating effect, as well as the energy input of the current hatch line were constant and the emerging melt pool exhibited the same shape. A constant lateral velocity v_{lat} not only implied a constant mean beam return time $\overline{t_{ret}}$ but also a constant minimum and maximum beam return time $t_{ret}^{max,min}$, as shown in Figure 5c. Since the local beam return time at each position of the hatch $t_{ret}(x, y)$ could be calculated from the linear relationship between the minimum and maximum beam return time, the absolute location of a defined return time, indicated in black, in Figure 5c was proportional to the line length. In the example shown in Figure 5c, the location changed from a 3.75 mm distance from the center of a scan length of $l_m = 10$ mm to a 11.25 mm distance from the center of a scan length of $l_m = 30$ mm. The relative position of the return time of interest was, however, constant at 87.5% of the scan length. As a result, turning point effects based on the same return time, as detailed in Figure 5c, changed their size as a function of line length, but their relative size remained constant.

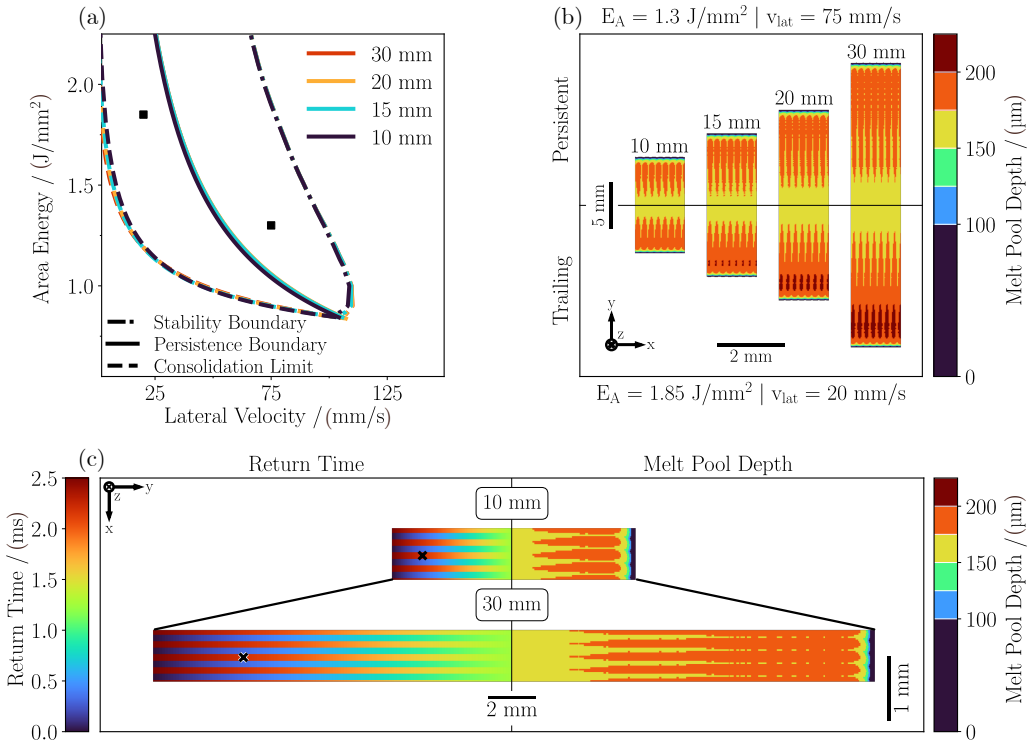

Figure 5. Processing boundaries for different scan lengths of 10, 15, 20, and 30 mm (**a**) for area energies of 0.6 J mm^{-2} to 2.2 J mm^{-2} and lateral velocities of 2.5 mm s^{-1} to 149.5 mm s^{-1} with a line offset of 100 µm, preheating temperature of 1023 K, and beam diameter of 200 µm. Corresponding melt pool depth distributions (**b**) for a parameter combination in the trailing regime with $E_A = 1.85\,\mathrm{J\,mm^{-2}}$ and $v_{lat} = 20\,\mathrm{mm\,s^{-1}}$ (**bottom**) and in the persistent regime with $E_A = 1.3\,\mathrm{J\,mm^{-2}}$ and $v_{lat} = 75\,\mathrm{mm\,s^{-1}}$ (**top**) for each line length. Local return times and local melt pool depth distributions (**c**) for two different line lengths for the first process parameter combination. The local return time, as well as the magnitude of the turning point effects, remained constant, but are scaled according to the line length.

Based on these results, melt pool geometries could be transferred between different scan lengths by establishing the same thermal conditions with the help of a constant area energy and lateral velocity, which could be accomplished by simultaneously increasing the beam power and velocity. However, significant changes in the beam power effected the beam diameter of the electron beam, since, depending on the used electron beam gun, the beam diameter changes as a function of the emitted beam power [55,56]. Therefore, the transfer and scaling of melt pool geometries to larger geometries with the help of higher beam powers can be challenging, due to the increased beam diameter and the respective shift of the processing boundaries.

3.5. Line Offset

The effect of different line offsets of 30 µm, 100 µm, and 150 µm on the melt pool depth distribution and the resulting processing boundaries is depicted in Figure 6a. At lower lateral velocities, the melt pool geometries emerging from a process parameter combination with a higher line offset exhibited a significantly higher melt pool depth and led to a shift of the consolidation boundary towards lower area energies and lateral velocities for higher line offsets. With increasing lateral velocities, however, this trend diminished. A higher line offset also led to a shift of the persistence boundary towards higher energy inputs and lateral velocities and, therefore, resulted in a larger trailing melt pool region. In contrast, the location and shape of the melt pool stability limit remained comparatively constant. Only the characteristic curvature at high lateral velocities shifted, along with the persistence and consolidation boundary, towards lower energies and higher lateral velocities for higher line offsets. While the persistent region of the processing map

elongated towards higher lateral velocities and lower area energies for higher line offsets, it simultaneously narrowed, due to the shift of the persistence boundary towards the upper right of the process parameter space.

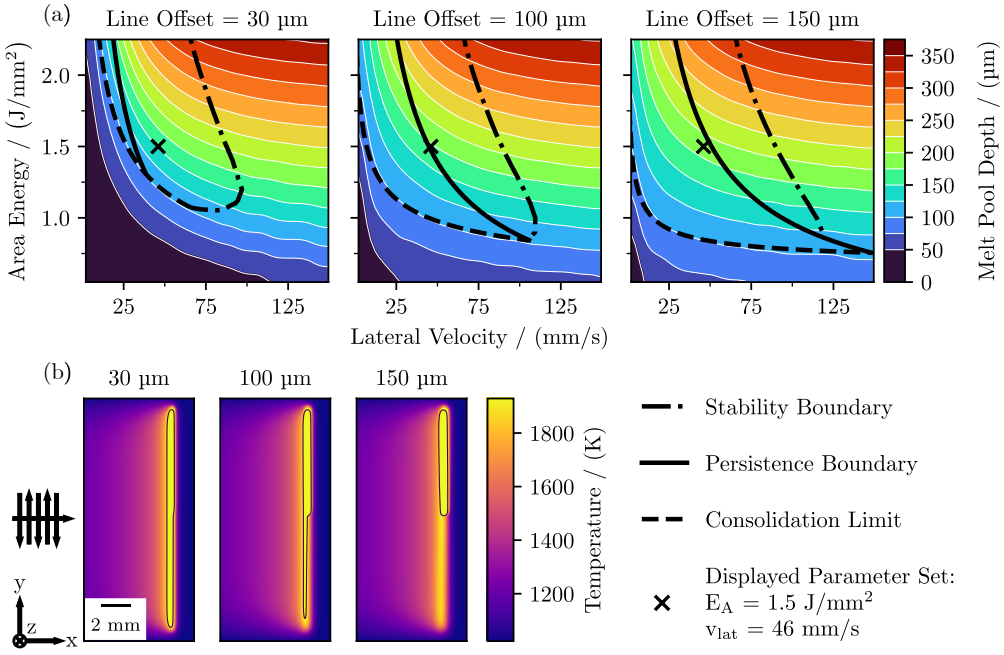

Figure 6. (**a**) Melt pool depth distributions and corresponding processing boundaries for various line offsets of 30 µm, 100 µm, and 150 µm using a beam diameter of 200 µm and a line length of 15 mm. (**b**) Emerging melt pool geometries of the indicated parameter set in (**a**), with the same area energy of 1.5 J mm^{-2} and a constant lateral velocity of 46 mm s^{-1}, but with varying line offsets.

In order to ensure a constant area energy E_A and lateral velocity v_{lat} using different line offsets, the beam velocity had to be adapted accordingly. A higher line offset required a lower beam velocity to maintain the lateral velocity, and consequently, the energy input of a single melt line, given by its line energy $E_l = P/v$, increased. As previously discussed in Section 3.3, melt pool formation in the trailing melt pool regime is mainly governed by the energy input of each single line. Therefore, process parameter combinations with a high line offset and high line energy exhibited a deeper melt pool in the trailing melt pool regime and the consolidation boundary shifted towards lower area energies and lateral velocities. In contrast, process parameter combinations with low line offsets had a lower line energy, and as a consequence the melt pool depth decreased significantly in the trailing melt pool regime, leading to a shift of the consolidation boundary towards higher energy inputs and lateral velocities, as shown in Figure 6a. These trends correspond well to experimentally observed trends for different line offsets [51,57]. The high beam velocity at low line offsets led to very low return times and a disproportionate increase in the cumulative heating effect with higher lateral velocities. This resulted in the formation of a line-like heat source [43]. Hence, the onset of the persistent melt pool regime shifted towards lower energy inputs. This effect was also reflected in the shape of the emerging melt pool, as depicted in Figure 6b for an exemplary parameter combination with an area energy of 1.5 J mm^{-2} and lateral velocity of 46 mm s^{-1}. While the process parameter combination with a low line offset of 30 µm showed the formation of a permanent persistent melt pool, the parameter combination with a high line offset of 150 µm was still located in the trailing melt pool regime. This behavior continued into the persistent melt pool regime, and the fundamental difference in the magnitude of line-based energy input and return time for different line offsets led to significant variations in the spatiotemporal melt pool formation. Parameter combinations with a low line offset exhibited an almost negligible

return time, and a stable and continuous line-shaped melt pool propagated over the surface as the result of multiple beam interactions at low line energy. The spatiotemporal evolution of the melt pool for parameter combinations with high line offsets, in contrast, was driven by longer return times. Therefore, the evolution was more dynamic and involved several solidification and remelting steps, especially at the turning points. In addition to return time based effects, the energy input of parameter combinations with a low line offset was based on multiple interactions with the low energy input. Therefore, the peak temperatures were lower compared to parameter combinations with high line offsets, resulting in a different evaporation behavior and melt pool dynamics [56].

The emergence of a unique melt pool geometry for each process parameter combination opened up the possibility of tailoring the material properties through the deliberate selection of the melt pool geometry, melt pool dynamics, and corresponding physical effects at the melt pool scale. Previous research has already established a variety of different relationships between final material properties and the required characteristic melt pool geometries, melt pool dynamics, and physical effects [12,39,56,57]. Appropriate process parameter combinations, resulting in the formation of the desired melt pool geometry, melt pool dynamics, and physical effects corresponding to the desired final material properties, can then be selected from the identified processing windows based on these existing melt pool–property relationships.

4. Summary and Conclusions

In order to establish process parameter–melt pool relationships, a comprehensive study of melt pool geometries in the quasi-stationary state of line-based hatching strategies was conducted, as a function of process parameters and processing conditions using high-throughput thermal simulations. Based on the emerging melt pool geometries, processing boundaries were identified, whose characteristic shape and relationship to each other enabled the precise identification of defect origins and the possibility of applying appropriate countermeasures in case of defect formation. In addition, this study provided guidelines for the effect of different processing conditions and processing strategies on the emerging melt pool geometries, the location of processing boundaries, and the final processing window. In general, this framework augments experimental process development with insights from high-throughput numerical simulations. It enables the selection of appropriate process parameters through process-parameter–melt pool relationships, in order to achieve the desired melt pool geometries according to melt pool–property relationships for already existing materials, as well as accelerating the development of processing parameters through the efficient design of experiments for new materials.

Author Contributions: Conceptualization, C.B., J.B. and C.K.; methodology, C.B., J.B. and C.K.; software, C.B. and J.B.; validation, J.B., C.B., M.M. and C.K.; formal analysis, C.B. and J.B.; investigation, C.B. and J.B.; resources, M.M. and C.K.; data curation, C.B.; writing—original draft preparation, C.B. and J.B.; writing—review and editing, C.B.; visualization, C.B., J.B. and C.K.; supervision, M.M. and C.K.; project administration, M.M. and C.K.; funding acquisition, M.M. and C.K. All authors have read and agreed to the published version of the manuscript.

Funding: This project received funding from the European Research Council (ERC) under the European Union's Horizon 2020 research and innovation program (grant agreement No 101018634). The authors gratefully acknowledge the HPC resources provided by the Erlangen National High Performance Computing Center (NHR@FAU) of the Friedrich-Alexander-Universität Erlangen-Nürnberg (FAU).

Data Availability Statement: Data supporting the findings of this study are available upon reasonable request from the corresponding author.

Conflicts of Interest: The authors declare no conflict of interest.

Appendix A. Material Properties

Table A1. Material properties for Ti6Al4V according to [34,46–48].

Property	Unit	Value
Thermal diffusivity	$m^2\,s^{-1}$	9×10^{-6}
Density	$kg\,m^{-3}$	4122
Specific heat	$J\,kg^{-1}\,K^{-1}$	670
Absorption coefficient		0.85
Liquidus temperature	K	1928

References

1. Del Guercio, G.; Galati, M.; Saboori, A.; Fino, P.; Iuliano, L. Microstructure and Mechanical Performance of Ti–6Al–4V Lattice Structures Manufactured via Electron Beam Melting (EBM): A Review. *Acta Metall. Sin.* **2020**, *33*, 183–203. [CrossRef]
2. Palmquist, A.; Jolic, M.; Hryha, E.; Shah, F.A. Complex geometry and integrated macro-porosity: Clinical applications of electron beam melting to fabricate bespoke bone-anchored implants. *Acta Biomater.* **2023**, *156*, 125–145. [CrossRef] [PubMed]
3. Yang, G.; Yang, P.; Yang, K.; Liu, N.; Jia, L.; Wang, J.; Tang, H. Effect of processing parameters on the density, microstructure and strength of pure tungsten fabricated by selective electron beam melting. *Int. J. Refract. Met. Hard Mater.* **2019**, *84*, 105040. [CrossRef]
4. Terrazas, C.A.; Mireles, J.; Gaytan, S.M.; Morton, P.A.; Hinojos, A.; Frigola, P.; Wicker, R.B. Fabrication and characterization of high-purity niobium using electron beam melting additive manufacturing technology. *Int. J. Adv. Manuf. Technol.* **2016**, *84*, 1115–1126. [CrossRef]
5. Fujieda, T.; Shiratori, H.; Kuwabara, K.; Kato, T.; Yamanaka, K.; Koizumi, Y.; Chiba, A. First demonstration of promising selective electron beam melting method for utilizing high-entropy alloys as engineering materials. *Mater. Lett.* **2015**, *159*, 12–15. [CrossRef]
6. Kirchner, A.; Klöden, B.; Franke-Jurisch, M.; Inarra Rauh-Hain, L.; Weißgärber, T. Manufacturing of Tool Steels by PBF-EB. *Metals* **2021**, *11*, 1640. [CrossRef]
7. Teschke, M.; Moritz, J.; Telgheder, L.; Marquardt, A.; Leyens, C.; Walther, F. Characterization of the high-temperature behavior of PBF-EB/M manufactured γ titanium aluminides. *Prog. Addit. Manuf.* **2022**, *7*, 471–480. [CrossRef]
8. Franke-Jurisch, M.; Mirz, M.; Wenz, T.; Kirchner, A.; Klöden, B.; Weißgärber, T. PBF-EB of Fe-Cr-V Alloy for Wear Applications. *Materials* **2022**, *15*, 1679. [CrossRef]
9. Lei, Y.; Aoyagi, K.; Chiba, A. A method to manipulate non-steady-state columnar-to-equiaxed transition in powder bed fusion additive manufacturing using an electron beam. *Acta Mater.* **2022**, *227*, 117717. [CrossRef]
10. Dehoff, R.R.; Kirka, M.; Sames, W.J.; Bilheux, H.; Tremsin, A.S.; Lowe, L.E.; Babu, S.S. Site specific control of crystallographic grain orientation through electron beam additive manufacturing. *Mater. Sci. Technol.* **2015**, *31*, 931–938. [CrossRef]
11. Raghavan, N.; Stump, B.C.; Fernandez-Zelaia, P.; Kirka, M.M.; Simunovic, S. Influence of geometry on columnar to equiaxed transition during electron beam powder bed fusion of IN718. *Addit. Manuf.* **2021**, *47*, 102209. [CrossRef]
12. Knörlein, J.; Franke, M.; Schloffer, M.; Körner, C. In-situ aluminum control for titanium aluminide via electron beam powder bed fusion to realize a dual microstructure. *Addit. Manuf.* **2022**, *59*, 103132. [CrossRef]
13. Shao, M.; Vijayan, S.; Nandwana, P.; Jinschek, J.R. The effect of beam scan strategies on microstructural variations in Ti-6Al-4V fabricated by electron beam powder bed fusion. *Mater. Des.* **2020**, *196*, 109165. [CrossRef]
14. Karapuzha, A.S.; Fraser, D.; Schliephake, D.; Dietrich, S.; Zhu, Y.; Wu, X.; Huang, A. Microstructure, mechanical behaviour and strengthening mechanisms in Hastelloy X manufactured by electron beam and laser beam powder bed fusion. *J. Alloys Compd.* **2021**, *862*, 158034. [CrossRef]
15. Juechter, V.; Scharowsky, T.; Singer, R.F.; Körner, C. Processing window and evaporation phenomena for Ti-6Al-4V produced by selective electron beam melting. *Acta Mater.* **2014**, *76*, 252–258. [CrossRef]
16. Guo, C.; Ge, W.; Lin, F. Effects of scanning parameters on material deposition during Electron Beam Selective Melting of Ti-6Al-4V powder. *J. Mater. Process. Technol.* **2015**, *217*, 148–157. [CrossRef]
17. Scharowsky, T.; Juechter, V.; Singer, R.F.; Körner, C. Influence of the Scanning Strategy on the Microstructure and Mechanical Properties in Selective Electron Beam Melting of Ti-6Al-4V. *Adv. Eng. Mater.* **2015**, *17*, 1573–1578. [CrossRef]
18. Moritz, J.; Teschke, M.; Marquardt, A.; Stepien, L.; López, E.; Brueckner, F.; Walther, F.; Leyens, C. Influence of Electron Beam Powder Bed Fusion Process Parameters at Constant Volumetric Energy Density on Surface Topography and Microstructural Homogeneity of a Titanium Aluminide Alloy. *Adv. Eng. Mater.* **2023**, 2201871. [CrossRef]
19. Arnold, C.; Pobel, C.; Osmanlic, F.; Körner, C. Layerwise monitoring of electron beam melting via backscatter electron detection. *Rapid Prototyp. J.* **2018**, *24*, 1401–1406. [CrossRef]
20. Pobel, C.R.; Arnold, C.; Osmanlic, F.; Fu, Z.; Körner, C. Immediate development of processing windows for selective electron beam melting using layerwise monitoring via backscattered electron detection. *Mater. Lett.* **2019**, *249*, 70–72. [CrossRef]

21. Liu, Q.; Wu, H.; Paul, M.J.; He, P.; Peng, Z.; Gludovatz, B.; Kruzic, J.J.; Wang, C.H.; Li, X. Machine-learning assisted laser powder bed fusion process optimization for AlSi10Mg: New microstructure description indices and fracture mechanisms. *Acta Mater.* **2020**, *201*, 316–328. [CrossRef]
22. Tapia, G.; Khairallah, S.; Matthews, M.; King, W.E.; Elwany, A. Gaussian process-based surrogate modeling framework for process planning in laser powder-bed fusion additive manufacturing of 316L stainless steel. *Int. J. Adv. Manuf. Technol.* **2018**, *94*, 3591–3603. [CrossRef]
23. Zhao, M.; Wei, H.; Mao, Y.; Zhang, C.; Liu, T.; Liao, W. Predictions of Additive Manufacturing Process Parameters and Molten Pool Dimensions with a Physics-Informed Deep Learning Model. *Engineering* **2023**, *23*, 181–195. [CrossRef]
24. Zhang, B.; Seede, R.; Xue, L.; Atli, K.C.; Zhang, C.; Whitt, A.; Karaman, I.; Arroyave, R.; Elwany, A. An efficient framework for printability assessment in Laser Powder Bed Fusion metal additive manufacturing. *Addit. Manuf.* **2021**, *46*, 102018. [CrossRef]
25. Aoyagi, K.; Wang, H.; Sudo, H.; Chiba, A. Simple method to construct process maps for additive manufacturing using a support vector machine. *Addit. Manuf.* **2019**, *27*, 353–362. [CrossRef]
26. Breuning, C.; Arnold, C.; Markl, M.; Körner, C. A multivariate meltpool stability criterion for fabrication of complex geometries in electron beam powder bed fusion. *Addit. Manuf.* **2021**, *45*, 102051. . [CrossRef]
27. Breuning, C.; Pistor, J.; Markl, M.; Körner, C. Basic Mechanism of Surface Topography Evolution in Electron Beam Based Additive Manufacturing. *Materials* **2022**, *15*, 4754. [CrossRef]
28. Gordon, J.V.; Narra, S.P.; Cunningham, R.W.; Liu, H.; Chen, H.; Suter, R.M.; Beuth, J.L.; Rollett, A.D. Defect structure process maps for laser powder bed fusion additive manufacturing. *Addit. Manuf.* **2020**, *36*, 101552. [CrossRef]
29. Breuning, C.; Markl, M.; Körner, C. A Return Time Compensation Scheme for Complex Geometries in Electron Beam Powder Bed Fusion. *Addit. Manuf.* **2023**, *76*, 103767. [CrossRef]
30. Zäh, M.F.; Lutzmann, S. Modelling and simulation of electron beam melting. *Prod. Eng.* **2010**, *4*, 15–23. [CrossRef]
31. Cheng, B.; Chou, K. Melt pool geometry simulations for powder-based electron beam additive manufacturing. In Proceedings of the 2013 International Solid Freeform Fabrication Symposium, Austin, TX, USA, 12–14 August 2013 ; University of Texas at Austin: Austin, TX, USA, 2013.
32. Tang, M.; Pistorius, P.C.; Beuth, J.L. Prediction of lack-of-fusion porosity for powder bed fusion. *Addit. Manuf.* **2017**, *14*, 39–48. [CrossRef]
33. Hashemi, S.M.; Parvizi, S.; Baghbanijavid, H.; Tan, A.T.; Nematollahi, M.; Ramazani, A.; Fang, N.X.; Elahinia, M. Computational modelling of process–structure–property–performance relationships in metal additive manufacturing: A review. *Int. Mater. Rev.* **2022**, *67*, 1–46. [CrossRef]
34. Rausch, A.M.; Küng, V.E.; Pobel, C.; Markl, M.; Körner, C. Predictive simulation of process windows for powder bed fusion additive manufacturing: Influence of the powder bulk density. *Materials* **2017**, *10*, 1117. [CrossRef]
35. Markl, M.; Rausch, A.M.; Küng, V.E.; Körner, C. SAMPLE: A Software Suite to Predict Consolidation and Microstructure for Powder Bed Fusion Additive Manufacturing. *Adv. Eng. Mater.* **2020**, *22*, 1901270. [CrossRef]
36. Zakirov, A.; Belousov, S.; Bogdanova, M.; Korneev, B.; Stepanov, A.; Perepelkina, A.; Levchenko, V.; Meshkov, A.; Potapkin, B. Predictive modeling of laser and electron beam powder bed fusion additive manufacturing of metals at the mesoscale. *Addit. Manuf.* **2020**, *35*, 101236. [CrossRef]
37. Plotkowski, A.; Ferguson, J.; Stump, B.; Halsey, W.; Paquit, V.; Joslin, C.; Babu, S.S.; Marquez Rossy, A.; Kirka, M.M.; Dehoff, R.R. A stochastic scan strategy for grain structure control in complex geometries using electron beam powder bed fusion. *Addit. Manuf.* **2021**, *46*, 102092. [CrossRef]
38. Stump, B.; Plotkowski, A. An Adaptive Integration Scheme for Heat Conduction in Additive Manufacturing. *Review* **2019**, *75*, 787–805. [CrossRef]
39. Pistor, J.; Breuning, C.; Körner, C. A single crystal process window for electron beam powder bed fusion additive manufacturing of a cmsx-4 type ni-based superalloy. *Materials* **2021**, *14*, 3785. [CrossRef] [PubMed]
40. Rubenchik, A.M.; King, W.E.; Wu, S.S. Scaling laws for the additive manufacturing. *J. Mater. Process. Technol.* **2018**, *257*, 234–243. [CrossRef]
41. Cacace, S.; Semeraro, Q. Fast optimisation procedure for the selection of L-PBF parameters based on utility function. *Virtual Phys. Prototyp.* **2022**, *17*, 125–137. [CrossRef]
42. Weaver, J.S.; Heigel, J.C.; Lane, B.M. Laser spot size and scaling laws for laser beam additive manufacturing. *J. Manuf. Process.* **2022**, *73*, 26–39. [CrossRef]
43. Plotkowski, A. Geometry-Dependent Solidification Regimes in Metal Additive Manufacturing. *Weld. J.* **2020**, *99*, 59S–66S. [CrossRef]
44. Stump, B.; Plotkowski, A.; Coleman, J. Solidification dynamics in metal additive manufacturing: Analysis of model assumptions. *Model. Simul. Mater. Sci. Eng.* **2021**, *29*, 035001. [CrossRef]
45. Nguyen, N.T.; Ohta, A.; Matsuoka, K.; Suzuki, N.; Maeda, Y. Analytical Solutions for Transient Temperature of Semi-Infinite Body Subjected to 3-D Moving Heat Sources. *Weld. J.* **1999**, *78*, 265-s.
46. Li, J.J.; Johnson, W.L.; Rhim, W.K. Thermal expansion of liquid Ti–6Al–4V measured by electrostatic levitation. *Appl. Phys. Lett.* **2006**, *89*, 111913. [CrossRef]
47. Welsch, G.; Boyer, R.; Collings, E. *Materials Properties Handbook: Titanium Alloys*; ASM International: Almere, The Netherlands, 1993.

48. Boivineau, M.; Cagran, C.; Doytier, D.; Eyraud, V.; Nadal, M.H.; Wilthan, B.; Pottlacher, G. Thermophysical properties of solid and liquid Ti-6Al-4V (TA6V) alloy. *Int. J. Thermophys.* **2006**, *27*, 507–529. [CrossRef]
49. Harris, C.R.; Millman, K.J.; van der Walt, S.J.; Gommers, R.; Virtanen, P.; Cournapeau, D.; Wieser, E.; Taylor, J.; Berg, S.; Smith, N.J.; et al. Array programming with NumPy. *Nature* **2020**, *585*, 357–362. [CrossRef]
50. Dalcin, L.; Fang, Y.L.L. Mpi4py: Status Update after 12 Years of Development. *Comput. Sci. Eng.* **2021**, *23*, 47–54. [CrossRef]
51. Pobel, C.R.; Osmanlic, F.; Lodes, M.A.; Wachter, S.; Körner, C. Processing windows for Ti-6Al-4V fabricated by selective electron beam melting with improved beam focus and different scan line spacings. *Rapid Prototyp. J.* **2019**, *25*, 665–671. [CrossRef]
52. Roos, S.; Rännar, L.E. Process window for electron beam melting of 316ln stainless steel. *Metals* **2021**, *11*, 137. [CrossRef]
53. Riensche, A.; Bevans, B.D.; Smoqi, Z.; Yavari, R.; Krishnan, A.; Gilligan, J.; Piercy, N.; Cole, K.; Rao, P. Feedforward Control of Thermal History in Laser Powder Bed Fusion: Toward Physics-based Optimization of Processing Parameters. *Mater. Des.* **2022**, *224*, 111351. [CrossRef]
54. Renner, J.; Breuning, C.; Markl, M.; Körner, C. Surface topographies from electron optical images in electron beam powder bed fusion for process monitoring and control. *Addit. Manuf.* **2022**, *60*, 103172. [CrossRef]
55. Reith, M.; Breuning, C.; Franke, M.; Körner, C. Impact of the Power-Dependent Beam Diameter during Electron Beam Additive Manufacturing: A Case Study with γ-TiAl. *Appl. Sci.* **2022**, *12*, 11300. [CrossRef]
56. Klassen, A.; Forster, V.E.; Juechter, V.; Körner, C. Numerical simulation of multi-component evaporation during selective electron beam melting of TiAl. *J. Mater. Process. Technol.* **2017**, *247*, 280–288. [CrossRef]
57. Gotterbarm, M.R. Kornstrukturmodifikation beim Selektiven Elektronenstrahlschmelzen der Nickelbasis-Superlegierung IN718. Ph.D. Thesis, Friedrich-Alexander-Universität Erlangen-Nürnberg (FAU), Erlangen, Germany 2022.